Dalton Transactions

Accepted Manuscript

This is an *Accepted Manuscript*, which has been through the Royal Society of Chemistry peer review process and has been accepted for publication.

Accepted Manuscripts are published online shortly after acceptance, before technical editing, formatting and proof reading. Using this free service, authors can make their results available to the community, in citable form, before we publish the edited article. We will replace this *Accepted Manuscript* with the edited and formatted *Advance Article* as soon as it is available.

You can find more information about *Accepted Manuscripts* in the Information for Authors.

Please note that technical editing may introduce minor changes to the text and/or graphics, which may alter content. The journal's standard Terms & Conditions and the Ethical guidelines still apply. In no event shall the Royal Society of Chemistry be held responsible for any errors or omissions in this *Accepted Manuscript* or any consequences arising from the use of any information it contains.

ROYAL SOCIETY OF CHEMISTRY

www.rsc.org/dalton

Synthesis, crystal and electronic structure of sodium metal phosphate for hybrid capacitor in non-aqueous electrolyte

Manickam Minakshi Sundaram*
Department of Chemistry, Murdoch University, Murdoch, WA 6150, ***Australia***

Teeraphat Watcharatharapong, Sudip Chakraborty, and Rajeev Ahuja
Department of Physics and Astronomy, Uppsala University, ***Sweden***

Shanmughasundaram Duraisamy, Penki Tirupathi Rao and Nookala Munichandraiah
Inorganic and Physical Chemistry, Indian Institute of Science, Bangalore 560012, ***India***

Abstract

Energy storage devices based on sodium have been considered as an alternative to the traditional lithium based system because of its abundance in nature, cost effectiveness and low environmental impact. The synthesis, crystal and electronic properties, because of the importance of electronic conductivity in supercapacitors for high rate applications, have been discussed. The density of states of mixed sodium transition metal phosphate (maricite, $NaMn_{1/3}Co_{1/3}Ni_{1/3}PO_4$) has been determined with the ab initio generalized gradient approximation (GGA) + Hubbard term (U) method. Computed results for the mixed maricite are compared with the band gap of parent $NaFePO_4$ and the electrochemical experimental results are in good agreement. Mixed sodium transition metal phosphate served as an active electrode material for hybrid supercapacitors. The hybrid device (maricite *versus* carbon) in non-aqueous electrolyte shows redox peaks in the cyclic voltammetry and asymmetric profiles in the charge-discharge curves while exhibiting 40 F/g and these processes are found to be quasi-reversible. After long term cycling, the device exhibit excellent capacity retention (95%) and coulombic efficiency (92%) of the initial performance. The presence of carbon and nanocomposite morphology identified through X-ray photoelectron spectroscopy (XPS) and transmission electron microscopy (TEM) studies ensures the high rate capability while offering possibilities to develop new cathode material for sodium hybrid device.

E: m.minakshi-sundaram@murdoch.edu.au

Dalton Transactions Accepted Manuscript

Introduction

Recently, supercapacitors (also named electrochemical capacitors or ultracapacitors) have been extensively studied as power sources for many electronic devices. Supercapacitors store larger amounts of energy than the traditional dielectric capacitors and deliver energy far faster than batteries. The electrochemical capacitors have higher power density with excellent coulombic efficiency over longer life time, nevertheless, they provide a lower energy density than their battery counterparts [1-2]. Despite of the lower energy density, electrochemical capacitors provide an opportunity for load levelling for energy storage. Supercapacitors are classified as symmetric, asymmetric and hybrid system. The most traditional type is symmetric system consisting of two identical carbon electrodes [3-5] relying on a double layer charging mechanism, and the system is called an electrical double layer capacitor (EDLC). Asymmetric capacitors incorporate dissimilar electrode exhibiting non-faradaic (EDLC) behaviour, while hybrid system comprises a porous carbon "capacitor type" electrode and a metal oxide "battery type" electrode. The asymmetric hybrid system is characterized by faradaic reactions (pseudo capacitance) and non-faradaic charge storage behavior (electrical double layer capacitance) which is a new class of energy storage device developed in recent years. The class of materials involve pseudocapacitance reactions are mainly electronically conducting polymers [6-8] and metal oxides [9-12]. Among the several oxides studied, asymmetric capacitors coupled with iron oxide (Fe_3O_4) and MnO_2 [7] seems to be the most promising. Till now, lithium (Li) based energy storage devices including both battery and capacitors have been extensively studied [9-14]. In terms of cost, availability and safety issues the most appealing alternative to lithium is to use sodium because the resource is abundant in nature. In this regard, results on sodium battery show promise as stationary storage devices for load levelling [15]. The success of MnO_2 as a cathode material for aqueous sodium battery and maricite $NaMPO_4$ (where M = Co, Ni or Mn) for aqueous hybrid

Dalton Transactions Accepted Manuscript

capacitor inspired the present investigation in non-aqueous solvents. The substitution of mixed metal cations in the parent $NaFePO_4$ maricite framework employed here is to overcome the poor electronic conductivity of iron containing phosphates and to have high rate capability.

Although supercapacitors are now available in the market, they still require improvements, in terms of energy and power densities, governed by the specific capacitance of the active electrode material and the cell voltage. Extensive research has been done on metal oxides such as manganese dioxide (MnO_2) [16], Iron oxide (Fe_2O_3) [17], Tin oxide (SnO_2) [18], Cobalt molybdenum oxide ($CoMoO_4$) [19], and Vanadium oxide (V_2O_5) [12] but to the best of our knowledge no work has been reported on olivine or Na analogue materials in non-aqueous electrolytes. Hence, with these factors as objectives, various strategies such as in-situ carbon coating on the active maricite electrode while using polymer as chelating agent in the sol-gel synthetic route, in-expensive and environment friendly Na analogue maricite electrode, and the use of non-aqueous solvent to increase the cell voltage has been reported in this work. The use of aqueous solution (i.e. KOH, LiOH, NaOH or Na_2SO_4) as electrolyte limits the cell potential to 2 V, beyond which water splitting occurs and hence the lower energy density (20 Wh/Kg). To overcome this, non-aqueous solution as electrolyte has been used to increase the voltage window to 3 V resulting in higher energy density (50 Wh/Kg). To our knowledge, no relevant research has been published in the literature on the sodium phosphate based electrode materials suitable for hybrid devices in non-aqueous solutions. Another objective of this study, because of the potential interest of this material, is to understand the importance of electronic conductivity through the theoretical study of its electronic structure within the density functional theory (DFT) in the generalised gradient approximation (GGA) + U method. The computed results show that the parent $NaFePO_4$ in its pure form has very poor conductivity; however, with mixed sodium transition metals the

Dalton Transactions Accepted Manuscript

conductivity has been significantly improved and found suitable for high-rate applications. The outline of the paper is as follows. Firstly, we detail the computational methods used in this study including structural parameter, density of states and relative energies. Secondly, the experimental methods employed in this study including physical and electrochemical results are presented.

Computational methods

The simulation and calculation have been performed using projector-augmented wave (PAW) implemented in the Vienna Ab-initio Simulation Package (VASP), which is based on Density Functional Theory (DFT) formalism. The plane wave cutoff of 500eV is reasonably sufficient to describe the electronic properties and has been tested well with the convergence criteria. In this work, all the optimized structures are fully relaxed by a conjugate-gradient (CG) algorithm so as to obtain the minimal total energy. The optimization is converged when an energy difference in each electronic step is less than 0.01 meV and the residue Hellmann-Feynman forces also reach 0.01 eV/Å in ionic relaxation. The 6x4x2 and 1x4x2 *k*-point grid generated by Monkhorst-Pack scheme [20] are used for pure and mixed sodium iron phosphate, respectively as a consequence of *k*-point convergence. Throughout the calculation, for the transition metals (TM) chosen (Fe, Co, Mn and Ni) 3p, 3d- and 4s-electrons are considered as valence electrons while for alkali metal (Na) atom 2p-electron has been taken as valence electron. The electron configurations of P and O are [Ar] $3s^2$, $3p^3$ and [He] $2s^2$, $2p^4$ in their PAW potentials, respectively. For the exchange correlational functional, Perdew Burke Ernzerhof (PBE) type Generalized Gradient Approximation (GGA) is used [21-22] to approximate non-linear exchange correlation term. The van der Waal correction proposed by Grimme [23] is also taken into consideration for incorporating the dispersion effect. Owing to the strong d-electron localization of transition metals, particularly, in phosphate materials, using pure DFT could result in self-interaction errors. In order to treat the localized 3d-

Dalton Transactions Accepted Manuscript

electron accurately, the standard Hubbard model (DFT+U approach) proposed by Dudarev *et al.* [24] is an important requirement and hence GGA+U has been employed in the calculation. The chosen U parameters are with reference [25] to the olivine structure Li*M*PO_4 where *M* = Fe, Mn, Co, and Ni (U_{Fe} = 3.71 eV, U_{Mn} = 3.92 eV, U_{Co} = 5.05, U_{Ni} = 5.26 eV) in which the effective U parameters were determined from a linear respond approach, and yielded the improvement in lattice parameters and cell volume corresponding to experimental results. To simulate the mixed sodium transition metal phosphate $NaMn_{1/3}Co_{1/3}Ni_{1/3}PO_4$ structure, the unit cell of parent sodium iron phosphate ($NaFePO_4$) has been enlarged by 3x1x1 and the preference site for those substitution atoms is likely to be the same site as iron atom. There are number of distinct structures that have been simulated by using the criteria of different TM−TM displacements and those results are discussed in the results and discussion.

Experimental

Sol–gel synthesis of $NaMn_{1/3}Co_{1/3}Ni_{1/3}PO_4$ was performed while mixing a stoichiometric amount of precursors containing sodium acetate, cobalt acetate, manganese acetate, nickel acetate, ammonium dihydrogen phosphate in double distilled water with an effective stirring. A unique synthetic approach is chosen to carbon coat the phosphate (maricite) particles using PVP as a source. The metal and phosphate reactants were dissolved in water at around 80° C and with a constant stirring, polyvinylpyrrolidone (PVP) was added to the solution as a chelating agent in 1:1 weight ratio to the metal ions. The pH of the solution was adjusted to 3.5 by adding nitric acid. The resulting sol was continued heating at 80 °C for an hour to obtain a viscous gel. Continuous stirring and heating the slurry resulted in complete evaporation of water and formation of thick gel. Then, the thick transparent gel was dried at 110 °C in hot air oven for 12 h. The obtained powder was calcined at 300 °C for 8 h and at 550 °C for 6 h in air with intermittent grinding. The resultant furnace cooled "maricite"

Dalton Transactions Accepted Manuscript

powder was ground for further analysis.

When PVP is added to the colloidal dispersion, the imide group (N and O atoms) establishes strong affinity to the metal colloidal dispersion. This bonding controls the particle growth and further heating this product at a higher temperature, polymer decomposes leaving carbon and nitrogen residues on the surface of mixed maricite. The presence of these residues reduces the particle size and consequently the reduction of the diffusion length to enhance the performance of the mixed maricite. The synthesized mixed maricite i.e. sodium phosphate ($NaMn_{1/3}Co_{1/3}Ni_{1/3}PO_4$) powders were subject to systematic physical and electrochemical studies. Powder X-ray diffraction (XRD) patterns were recorded on X-ray diffractometer (Bruker D8 advance diffractometer) with a Cu Kα radiation (λ = 1.5418 Å) source. The microscopy studies were carried out using a scanning electron microscopy (FEI Co. Sirion) and transmission electron microscopy (JEOL TEM 2100F). Surface area and pore size distribution of the samples were measured using Micromeritics surface area analyser (model ASAP 2020). The surface elements on the maricite was examined by X-ray photoelectron spectroscopy (XPS) using a SPECS GmBH spectrometer (Phoibos100MCD Energy Analyser) with MgKα (1253.6 eV) radiation. The peak of C (1s) at 286 eV was taken as the reference energy position.

All electrochemical studies were carried out in a coin cell (CR2032, Hohsen Corporation, Japan). Maricite powder coated on stainless steel disc as current collector was used as cathode. The "commercial carbon powder" (YEC8) used in this study was "as-received" form purchased from Fuzhou Yi Huan Carbon Co. Ltd., China. Carbon powder or Sodium metal foil (Aldrich) was used as counter and reference electrodes. The stainless steel disc was polished with successive grades of emery, degreased, etched in dilute 10% HNO_3 and 10% HCl, washed with detergent and rinsed with distilled water and acetone followed by drying in air. The active material (maricite powder, 75 wt %), conductive material (Ketjen black, 15 wt %) and polyvinylidene fluoride (PVDF, 10 wt %) were mixed and ground in a

Dalton Transactions Accepted Manuscript

mortar. Few drops of n-methyl pyrrolidinone (NMP) were added to form slurry. The slurry was coated on the pre-treated stainless steel foil until getting the required loading level and dried the coated disc at 100 °C under reduced pressure for 12 h. Carbon electrode disc was prepared in an identical manner except the inclusion of conductive material. The coin cell was constructed with the sodium phosphate disk as the cathode, carbon as the anode and Celgard porous propylene membrane (2400) as the separator. The optimal mass ratio between sodium phosphate ($NaMn_{1/3}Co_{1/3}Ni_{1/3}PO_4$) and commercial carbon was determined to be 1.5 for the fabricated hybrid ($NaMn_{1/3}Co_{1/3}Ni_{1/3}PO_4$|| commercial carbon) capacitor. The mass balance was calculated using the following equation (1)

$$m+ /m- = (C_- * \Delta E_-) / (C_+ * \Delta E_+) \quad \text{Eq. [1]}$$

where C is the specific capacitance; ΔE is the potential window for the charge / discharge processes. The mass of the positive and negative electrode material was 2.0 and 3.0 mg, respectively. Coin cells were assembled in an argon filled glove box MBraun model UNILAB. A non-aqueous solution of 1M $NaPF_6$ dissolved in ethylene carbonate, diethyl carbonate and dimethyl carbonate (2:1:2 v/v) electrolyte was used as an electrolyte. An aliquot (5 µL) of non-aqueous electrolyte was added on to the separator. The cyclic voltammetry (CV) and galvanostatic charge-discharge cycling were measured by a Biologic SA multichannel potentiostat/galvanostat model VMP3. The electrochemical impedance spectroscopy (EIS) measurements were carried out on the maricite electrodes before and after electrochemical cycling experiments at open-circuit potential in the frequency ranging from 0.01 Hz to 100 kHz with an a. c. excitation amplitude of 5 mV by Solatron frequency response analyser model 1255B and Solatron electrochemical interface model 1287.

Dalton Transactions Accepted Manuscript

Results and Discussion

1. Crystal structure and density of states

(a) Pristine m-$NaFePO_4$

The *maricite*-$NaFePO_4$ (*m*-$NaFePO_4$) structure containing 28 atoms is constructed and optimized using the convergence criteria mentioned earlier in the introduction section. The crystal structural parameters of pure $NaFePO_4$ have been showed in table 1 obtained from the Figure 1 for both the effective U_{Fe} and an arbitrary value of 5.3 eV. The experimental values are also compared in the table 1. We have found a good correspondence between the calculated results and the experimental values after the Hubbard U was introduced. It is worth mentioning that there is a substantial volume expansion when a higher U value is considered. In this work, U_{Fe} = 3.71eV is the value that we have mainly taken into account for the electronic structure calculation as it yields the cell parameters which is close to the experimental ones.

The density of state calculations as depicted in Figure 2 show the significant effect of onsite coulomb interaction in the electronic structure, which leads to more reasonable band gap. The *m*-$NaFePO_4$ is known as an indirect gap semiconductor, but it can be distinctly seen that the conduction band drops and crosses the Fermi level indicating that Perdew Burke Ernzerhof (PBE) functional cannot predict the electronic properties correctly due to the under estimated localization of Fe 3*d*-electrons. We have found the band gap (E_g) for U values 3.71 and 5.3 eV as 2.99 and 3.84 eV respectively. Although a larger E_g can be obtained using a higher U parameter, the density of state (DOS) results (shown in Fig. 2) appears to be still identical. The Figure 2b shows that the valence and conduction bands are mostly attributed to the hybridization of Fe-3*d* and O-2*p* orbitals. In the experimental study of Avdeev *et al.* [26], for the identical material, the local structure of FeO_6 octahedra was found to exhibit the elongation Jahn-Taller effect leading to the Fe-O longer axial bonds. Moreover, we theoretically found *m*-$NaFePO_4$ is characterized by an antiferromagnetic ground state with

Dalton Transactions Accepted Manuscript

the Fe local magnetic moment of 3.71 μ_B in good agreement with the experiment value of 3.89 μ_B [26]

(b) Mixed sodium transition metal phosphate (m-$NaMn_{1/3}Co_{1/3}Ni_{1/3}PO_4$)

To determine the density of states for mixed maricite $NaMn_{1/3}Co_{1/3}Ni_{1/3}PO_4$, the pristine *m*-$NaFePO_4$ is mixed with Mn, Co and Ni atoms replacing on Fe sites individually with the fractional occupancy of 0.33 and the iso-structures are shown in Figure 3. Here, three different *m*-$NaMn_{1/3}Co_{1/3}Ni_{1/3}PO_4$ structures are termed as C1, C2 and C3 configurations. The three configurations have been differentiated by the magnitude order of average TM−TM (transition metal) distance (tabulated in Table 2), e.g. Mn−Mn distance, where C1 and C3 structures have the shortest and longest distance, respectively, as noticed in Figure 3.

Among the three different configurations, in Fig. 3, the C3 structure has the lowest total energy compared to C2 and C1. This indicates that the TM (Ni) atom prefers to reside apart from each other and the consequent configuration is energetically favorable. This can also be explained by the charge distribution. Since the number of electrons to be donated is different, the way the TM atom residing on a specific site should also influence the electron distribution within the respective structure. The homogeneity of the charge distribution of the C3 configuration makes the structure more stable compared to C1 and C2 configurations. Based on the relation of the total energy and structural stability, the C1 and C3 are energetically favorable in ferromagnetic ground states with the different total energies between two distinct magnetic orderings of 0.77 and 13.97 meV/formula higher than in antiferromagnetic spin ordering, respectively. Whereas, the C2 is likely to be antiferromagnetic and possibly manifests ferromagnetism owing to very small value of such energy (0.12 meV/formula). This shows the magnetic ordering is also related to the stability of the respective structures. Even so, in order to perceive the difference between them, the results of their DOS are all plotted in Figure 4. The Fermi level (E_f) of all the DOS has been

Dalton Transactions Accepted Manuscript

set at 0 eV and we have found that the main contributions of DOS in mixed $NaMn_{1/3}Co_{1/3}Ni_{1/3}PO_4$ originates from O-2*p*, Mn-3*d* Co-3*d* and Ni-3*d* orbitals and the Na and P atoms have weak density of states in the energy range of -10.5 and 10.5 eV. The conduction band occurs from the 3d-electrons of TM atoms. As seen in Figure 4, independent of TM atom location, Ni-3*d* electrons play an essential role on the edge of the conduction band as well as the valence band, which is mostly dominated by the 2*p*-electrons of O and has the hybridized O-2*p* and Mn-3*d* character at the edge of valence band. The observed smaller E_g ($\sim 2.24 - 2.32$ eV) of *m*-$NaMn_{1/3}Co_{1/3}Ni_{1/3}PO_4$ suggests the electrical conductivity is improved after mixing with various TM's such as Mn, Co, and Ni. Moreover, at the near core energy states, there are small peaks of Ni, Co and Mn atoms corresponding to their (3p-states) appear in the energy order of Ni < Co < Mn. The relatively smaller band gap observed for the mixed sodium transition metal phosphate is consistent with its improved electrochemical activity, discussed in the electrochemical characterization section. The X-ray photoelectron spectroscopy (XPS) spectrum describing the activation energy to excite electrons in core region (detailed in the physical characterization section) shows the similar order of energy states as we found in lower energy range of DOS for the mixed metal phosphate. Comparing the DOS of each configuration, in Figures 4, they look quite similar but have the different spin-up and down. The computed method led to comparable results between the experimental XPS spectrum and the calculated total DOS of mixed sodium transition metal phosphate.

2. Experimental measurements of m-$NaMn_{1/3}Co_{1/3}Ni_{1/3}PO_4$

(a) Physical characterization

The X-ray diffraction analysis (XRD) carried out on the synthesized mixed maricite $NaMn_{1/3}Co_{1/3}Ni_{1/3}PO_4$ powder evidences a well-defined diffraction lines with high diffraction intensities ascertaining a crystalline structure of the material. Figure 5 shows the XRD patterns of the maricite, all peaks can be indexed to orthorhombic Na*M*PO_4 analogue (JCPDS

Dalton Transactions Accepted Manuscript

card no. 71-5040, ICDD no. 29-1216; *Pmna* space group) based on the maricite mineral. It is also important to note that the synthesized so-called maricite phase exhibits lattice parameters higher than those of the Li analogue [27]. This difference is attributed to the larger ionic ratio of Na^+ with respect to the Li^+ counterpart i.e. 1.02 Å vs. 0.76 Å, respectively [28-29]. As each of the metal cation dopant (Mn, Co and Ni) has an ionic radius in octahedral coordination comparable to that of the parent Fe^{2+} [30], a preference for this site is expected and the material crystallised in a single phase without any detectable impurities or second phase. To aid this fact, X-ray photoelectron spectroscopy (XPS) analysis is also performed on the maricite powder (discussed later in this section).

The N_2 adsorption isotherms and pore size distribution curves of the mixed maricite $NaMn_{1/3}Co_{1/3}Ni_{1/3}PO_4$ powder are presented in Fig. 6. The surface area of the sample was calculated using the Brunauer-Emmett-Teller (BET) method, while the pore size distribution and pore volume were calculated from the desorption based on the Barrett-Joyner-Halenda (BJH) equation. The surface area measured from the BET isotherm for mixed maricite was found to be 5 m^2/g. The typical nitrogen sorption isotherms exhibit type IV isotherms with a typical hysteresis loop in the intermediate relative pressure range (0.7 – 0.9). The pore size (shown in the inset, Fig. 6) shows a uniform distribution of around 60 nm, illustrating the formation of mesoporous material. Although the surface area (5 m^2/g) of synthesized maricite is much lower than that of reported materials for oxide, phosphate and molybdate counterparts i.e., MnO_2 (16 m^2/g) [16], reduced graphene oxide/MnO_2 (49 m^2/g) [31], TiP_2O_7 (12 m^2/g) [32], $NiMoO_4$ (15 m^2/g) [33], graphene added $MnMoO_4$ (~ 10 m^2/g) [34] but it is comparable to that of other olivine/maricite materials Na_2FePO_4F (8.7 m^2/g) [35] and $LiFePO_4$/C (5.2 m^2/g) [36]. The surface area for commercial carbon electrode was observed to be 1450 m^2/g with a high porosity of 0.76 cm^3/g. The high surface area and controlled distribution of pores obtained for both the electrodes, determine the electrode/electrolyte

Dalton Transactions Accepted Manuscript

interface in supercapacitor applications that facilitates the EDL capacitance and faradaic capacity [37-38]. Hence, high specific area together with a narrow pore size distribution of carbon coupled with crystalline structure of maricite (battery like electrode) is suffice to achieve high capacitive performance, demonstrated in the following section.

The Scanning electron microscope images in Fig. 7 show the morphology of the synthesized mixed maricite $NaMn_{1/3}Co_{1/3}Ni_{1/3}PO_4$ powder that appears to be porous with voids having individual grain size of 0.4 – 0.6 μm. At the macroscopic scale, electrode homogeneity and integrity have been important in ensuring active material performance. Energy dispersive X-ray Spectroscopy (EDS) analysis carried out on various locations of maricite powder showed very similar spectra confirming the high homogeneity of the material. A representative spectrum of this analysis is reported in Fig. 8. EDS analysis confirms the presence of elements present in the material. The presence of all transition metal cation and sodium peak positions support the XRD pattern that the substitution of multiple dopants crystallises in a single phase compound. The quantitative amount of carbon (from CHNS analysis) in the synthesized maricite was found to be 2.15 wt% of the material. This confirms the carbon has been present on the synthesized maricite particle that could provide the electronic conductivity and play as percolator between the grains. The evidence for carbon coating on the maricite material, surface morphology and crystalline nature of synthesized maricite powder were also investigated by X-ray photoelectron spectroscopy (XPS), transmission electron microscopy and high resolution (TEM & HRTEM) measurements. A survey scan XPS of the surface (0 – 1200 eV) of the synthesized mixed maricite powder is shown in Fig. 9a. The important feature to notice in the wide spectrum is the highly dominant O (1s) and Na (1s) peaks, while the contributions of other elements of interest (Mn, Co, Ni and P) corresponding to mixed transition metal phosphates are also seen but weak in their intensities. To confirm the presence of carbon coating on the surface of as-

Dalton Transactions Accepted Manuscript

synthesized maricite, the XPS spectrum over C (1s) were recorded over five sweeps and shown in Fig. 9b. Based upon binding energies as reported in the literature [39-41], the C (1s) peaks were assigned at 286 eV to hydrocarbon present in the XPS chamber (taken as charge referencing) and the second peak at 282 eV to carbon present in the maricite material itself, comes from PVP. The peak fitting was done by applying multiple Gaussians. The composition of surface elements from XPS profiles further confirms the role of PVP and its carbon coating on the maricite surface. While the XPS analysis provides an indication of the composition of elements present on the surface including carbon, CHNS measurements are an indication of the concentration of the C element in the whole mixed maricite powder. We found that both the techniques are complimentary and quantitatively the amount of C is found to be 2.15 wt. % of the material. Figure 10 exhibits TEM images of the maricite nanocomposites showing a carbon coating on the active material and are seen as clusters. The polymer polyvinylpyrrolidone (PVP) from the chelating agent during the sol-gel synthesis allows unique control over the particle growth and the composites in nanometre range having small dimensions to facilitate electron and ion transport. PVP an electrically conducting polymer can form a conducting matrix having particle to particle interaction and acts as a backbone in the poorly conducting maricite material. The role of PVP also acts as a template for the formation of unique (flexible-type) shape of the particles shown in the TEM images [42]. The presence of carbon coating on the maricite surface (as evidenced from XPS and EDS analyses) may accelerate the diffusion reaction on the surfaces of the maricite material [43]. The TEM images also possess a porous nature confirming the SEM morphology which will enhance the electron/ion transportation for better electrochemical reactions. The HRTEM image further confirms the crystallinity of the obtained product and carbon particles on the surface evidenced through series of ring and diffraction spots. The carbon layer may improve electronic conductivity and shorten the sodium-ion diffusion paths.

Dalton Transactions Accepted Manuscript

(b) Electrochemical characterization

Asymmetrical hybrid device is constructed with mass loadings, as specified in the experimental section, of sodium phosphate nanocomposites versus commercial carbon ($NaMn_{1/3}Co_{1/3}Ni_{1/3}PO_4$ || carbon) as positive and negative electrodes, respectively. They were characterised by cyclic voltammetry, galvanostatic charge-discharge and electrochemical impedance spectroscopy. In the case of conventional symmetric capacitors [1, 3] (activated carbon *vs*. activated carbon), during charge and discharge, an electrochemical double layer is found to be reversibly formed on the electrodes. The anion and cation species (Na and PF_6^-) from the electrolyte adsorb on the positive and negative electrodes, respectively during charge process. Such non-faradaic processes lead to low capacitance of only 10 F/g [1]. In the hybrid device, on the other hand, mixed maricite electrode exhibits battery type of behavior. The hybrid capacitor (mixed maricite *vs*. carbon) utilise double-layer capacitance on the carbon, which occurs in parallel with a faradaic process at the maricite [44]. The faradaic process involves redox reactions of electrochemically active maricite species at the electrode particle surface [45]. The intercalation and double-layer adsorption are the two reactions which we have observed in our asymmetrical hybrid device, totalling 40 F/g, which is explained in the following discussion on galvanostatic and potentiostatic experiments. The capacitance (C) is calculated from the discharge profiles according the equation $C = I\Delta t / m \Delta V$, where I is the constant discharge current, Δt is the discharge time, m is mass of the active maricite material and ΔV is the potential window for discharge.

Cyclic voltammogram recorded for the cathode i.e. mixed maricite $NaMn_{1/3}Co_{1/3}Ni_{1/3}PO_4$ electrode versus commercial carbon at two different potential sweep rates of 1 and 100 mV/s in the potential window of 0 and 3 V are presented in Fig. 11. Initially, the electrode was swept in an anodic (oxidation) direction until the cut-off voltage and then reversed back in the cathodic (reduction) direction to the initial voltage. The current

Dalton Transactions Accepted Manuscript

response of the higher scan rate is superior when compared to the sample at a lower scan rate indicating that the synthesised maricite has a better capacitance behavior. At a low scan rate (Fig. 11a), voltammogram shows a weak anodic peak around 2.5 V during the forward scan related to the oxidation of a redox couple. In the reverse scan, two clear reduction current peaks are observed at 1.7 and 0.4 V, respectively. From one of our earlier studies [46] based on Na*M*PO_4 (where *M* = Co, Ni or Mn) it is inferred that the weak reduction peak at 1.7 V (Fig. 11a) is due to the reduction of Co^{3+} and the intense peak at 0.4 V is due to the reduction of Ni^{3+} and Mn hasn't taken part in the redox activity. On the basis of cyclic voltammetric data, the reaction thus proposed for the charge/discharge processes of maricite is as follows:

$$NaMn_{1/3}Co_{1/3}Ni_{1/3}PO_4 \underset{\text{Discharge}}{\overset{\text{charge}}{\rightleftharpoons}} Na_{1-x}Mn_{1/3}Co_{1/3}Ni_{1/3}PO_4 + x\,Na^+ + x\,e^- \quad \text{Eq. [2]}$$

(battery type)

The proposed reaction for the commercial carbon is

$$C + xNa^+ + xe^- \leftrightarrow C^{x-} \,||\, xNa^+ \qquad \textit{(capacitor type)} \qquad \text{Eq. [3]}$$

In addition to the proposed Na absorption reaction in eq. (3) electric double layer with the anion, PF_6^- from the electrolyte could not be ruled out.

The redox peaks observed in Fig. 11a are found to fully reversible for successive cycles indicating a reversible dominant faradaic behavior. As the scan rate was increased to 100 mV/s (Fig. 11b), a clear deviation from the battery type (faradaic) behavior to capacitive (non-faradaic) EDL behavior is observed [47]. No distinct redox peaks were observed for higher sweep rates. This suggests that at low scan rates the diffusion controlled process can proceed with sodium-ion de-insertion and insertion into almost all of the available pores in the maricite structure (showed in the SEM and TEM images, Figs 7 & 10) resulting in pseudo capacitive behavior but with less capacitance. As higher scan rates were achieved (in Fig. 12), the surface of the electrode results in a large reduction and hence the observed high

Dalton Transactions Accepted Manuscript

current response. The absence of well-defined redox peaks could be related to difficulties in ion diffusion inside the pores at high current densities ≥ 20 mV/s (Fig. 12). Hence, at very low scan rates, faradaic character is clearly indicated by redox peaks on the CV while a quasi-rectangular shape close to that expected for a pure electrochemical double layer capacitor with some contribution to faradaic process is observed for very high scan rates [37, 48]. From these results, it is established that higher current may lead to pure capacitive behavior without pseudocapacitive contribution and hence only optimal lower current was selected for further charge-discharge studies.

The supercapacitive performance was demonstrated by the galvanostatic charge-discharge experiments and those profiles for multiple cycles are shown in Fig. 13a-b. The operating voltage range (0 – 3.0 V) is in agreement with the cyclic voltammetric data. The device exhibit charge-discharge profiles (in Figs. 13a-b) slightly deviating from linearity as a result of the pseudo-faradaic processes for the phosphate electrodes. The bent like curve (instead of straight lines) at the higher and lower potentials suggests that partial Na^+ ion insertion/extraction occurs [49] in the maricite electrode. The overall capacitance contribution of the maricite electrode comes from both the capacitive and battery – like behaviour comprising 40 F/g. The obtained capacitance values are comparable to that of the reported values for sodium and lithium-ion capacitors [4, 31, 35, 50-51]. Their stability upon cycling was investigated and the Fig. 15b shows that the reversibility can be achieved with the $NaMn_{1/3}Co_{1/3}Ni_{1/3}PO_4$ versus commercial carbon electrochemical supercapacitor. Figure 13c shows the cycleability and coulombic efficiency of the hybrid device. The available capacitance remained constant throughout the tested cycling period of 1000 cycles exhibiting 38 F/g with an excellent coulombic efficiency of 92%. The exhibited excellent cyclability could be attributed to the role of Mn in stabilising the structure for longevity. As reported by Amine et al [52] for manganese layered oxide and Kang et al [53] for manganese mixed

Dalton Transactions Accepted Manuscript

phosphate, Mn achieves cycling stability at the expense of low capacitance. This is explained as due to the unique Jahn-Teller distortion of Mn^{3+}, which mitigates the diffusion channel for reversibility. The designed hybrid device can deliver energy density 50 Wh/Kg at a power density of 180 W/Kg. The power density (P_d) and energy density (E_d) of the hybrid device are calculated from the capacitance value obtained from the charge-discharge profiles using the relations, P_d (W Kg^{-1}) = ($\Delta E \cdot I / m$) and E_d (Wh/Kg) = ($P_d \cdot t / 3600$) where ΔE = (E_{max} + E_{min})/2 and E_{max} and E_{min} are, respectively, the voltage at the start of discharge and at the end of discharge, *t* the time taken for charge/discharge, *I* the applied current and *m* the weight of active material in the electrode [54].

Electrochemical impedance spectroscopy (EIS) was performed on assembled hybrid device at the open circuit voltage and after multiple galvanostatic cycles. EIS is a powerful tool to investigate the electrochemical behaviours at the bulk and interface of the device and to determine the degree to which ions access through the surface at specific frequencies [55-56]. Figure 14 showed the Nyquist plots of the $NaMn_{1/3}Co_{1/3}Ni_{1/3}PO_4$ versus commercial carbon device, in the frequency range from 100 kHz to 100 mHz. It can be observed that for the open circuit potential, the plot is composed of a small diameter of the semicircle in the high-frequency range corresponding to the charge transfer processes occurring at the electrode/electrolyte interface [57-58] and an inclined line at 90° corresponding to the impedance of Na^+ diffusion process. The line close to 90° was attributed to the ideal capacitive behaviour [59]. The observed low ohm resistance (high frequency intersect with the real axis) corresponds to the electrolyte resistance and the much loss of lines with slope of 90° portion indicates Warburg resistance is negligible reflecting the synthesized maricite is a highly porous electrode and apt for hybrid devices. Comparing the plots after multiple cycles, it is apparent that a greater charge transfer resistance is observed (Fig. 14, inset) and the slope changed from 90° towards lower angle and a minor variation in ohm resistance. These

Dalton Transactions Accepted Manuscript

changes are due to the faradaic and non-faradaic reactions at the interface during the charge/discharge process and the ion transport from the electrolytes into the electrode [60]. Hence, the obtained EIS spectrum is in accordance with the other electrochemical results.

Conclusions

In summary, our theoretical and experimental studies of mixed sodium metal phosphate reveal improved electronic conductivity with a lower band gap than the parent $NaFePO_4$. The density of states spectrum for the metal phosphate is consistent with the experimental results exhibiting improved performance. Asymmetric hybrid device, $NaMn_{1/3}Co_{1/3}Ni_{1/3}PO_4$ versus commercial carbon, showed a discharge capacitance of 40 F/g in non-aqueous electrolyte. The charge-discharge curve maintained a triangular bent curve at a current of 0.25 mA and the electrode exhibited a low ohm resistance with excellent reversibility. The maricite electrode shows dominant Na^+ insertion/extraction (Faradaic) behavior at the low sweep rate while dominant adsorption/desorption (non-Faradaic) behavior at the high sweep rate voltage window 0 – 3.0 V. The capacity retention and coulombic efficiency of the hybrid device maintains 95% and 92% respectively during the multiple cycling, indicating a high electrochemical reversibility. The presence of mesopores, carbon coated maricite enhanced the electrochemical performance in terms of excellent stability over the cycling period. The sodium derived electrode material is found to be suitable for energy device applications.

Acknowledgements

The author (MMS) wishes to acknowledge the funding bodies, Australia-India Strategic Research Fund (AISRF) and Australian Research Council (ARC). This research was supported under Australian Research Council (ARC) Discovery Project funding scheme DP1092543 and Australia-India Early Career Research Fellowship. Authors TW, SC and RA would like to acknowledge the Carl Tryggers Stiftelse for Vetenskaplig Forskning (CTS),

Dalton Transactions Accepted Manuscript

Swedish Research Council (VR), Swedish Energy Agency and Development and Promotion of Science and Technology Talents Project (DPST) promoted by the Royal Thai Government. SNIC, HPC2N and UPPMAX are also acknowledged for the computing time

References

1. M. Winter and R. J. Brodd, *Chem. Rev.*, **2004**, 104, 4245.
2. Z. -L. Wang, D. Xu, H. -G. Wang, Z. Wu and X. -B. Zhang, *ACS Nano*, **2013**, 7, 2422.
3. L. Li, Z. Wu, S. Yuan and X. -B Zhang, *Energy Environ. Sci.*, **2014**, 7, 2101.
4. B. Fang, A. Bonakdarpour, M. – S. Kim, J. H. Kim, D. P. Wilkinson and J. –S. Yu, *Microporous and Mesoporous Mater*. **2013**, 182, 1.
5. M. Nakamura, M. Nakanishi, K. J. Yamamoto, Power Sources, **1996**, 60, 225
6. A. Rudge, J. Davey, I. Raistrick, S. Gottesfeld and J. P. Ferraris, *J. Power Sources*, **1994**, 47, 89.
7. F. Fusalba, N. El. Mehdi, L. Breau and D. Belanger, *Chem. Mater.* **1999**, 11, 2743.
8. E. Naudin, H. A. Ho, S. Branchaud, L. Breau and D. Belanger, *J. Phys. Chem. B.*, **2002**, 106, 10585.
9. H. Kim and B. N. Popov, *J. Power Sources*, **2002**, 104, 52.
10. K.-H. Chang and C.-C. Hu, *J. Electrochem. Soc*, **2004**, 151, A958.
11. P. Soudan, J. Gaudet, D. Guay, D. Belanger and R. Schulz, *Chem. Mater.*, **2002**, 14, 1210.
12. H. Y. Lee and J. B. Goodenough, *J. Solid State Chem.*, **1999**, 144, 220.
13. A. Brandt and A. Balducci *Electrochim. Acta*, **2013**, 108, 219.
14. S. R. Sivakkumar and A. G. Pandolfo, *Electrochim. Acta*, **2012**, 65, 280.
15. A. Abouimrane, W. Weng, H. Eltayeb, Y. J. Cui, J. Niklas, O. Plouektov and K. Amine, *Energy and Environ. Sci*., **2012**, 5, 9632.
16. M. Toupin, T. Brousse and D. Belanger, *Chem. Mater*., **2004**, 16, 3184.
17. T. Brousse and D. Belanger, *Electrochem. Solid State. Lett*., **2003**, 6, A244.
18. K. R. Prasad and N. Miura, *Electrochem. Commun*., **2004**, 6, 849.
19. R. Ramkumar and M. Minakshi, *Dalton Trans.*, **2015**, 44, 6158.
20. H. J. Monkhorst and J. D. Pack, Phys. Rev. B., 1976, 13, 5188.
21. P.E. Blochl, *Phys. Rev. B*., **1994**, 50, 17953.
22. G. Kresse and D. Joubert, *Phys. Rev. B.*, **1999**, 59, 1758.

Dalton Transactions Accepted Manuscript

23. S. Grimme, *J. Comput. Chem*., **2006**, 27, 1787.
24. S. L. Dudarev, G. A. Botton, S. Y. Savrasov, C. J. Humphreys and A. P. Sutton, *Phys. Rev. B*., **1998**, 57, 1505.
25. F. Zhou, M. Cococcioni, K. Kang and G. Ceder, *Electrochem. Commun*. **2004**, 6, 1144.
26. M. Avdeev, Z. Mohamed, C. D. Ling, J. Lu, M. Tamru, A. Yamada and P. Barpanda, *Inorg. Chem*. **2013**, 52, 8685.
27. M. Minakshi, S. Kandhasamy and D. Meyrick, *J. Alloys and Compds*. **2012**, 544, 62.
28. B. L. Ellis, W. R. M. Makahnouk, Y. Makimura, K. Toghill and L. F. Nazar, *Nature Mater*., **2007**, 6, 749.
29. J. P. Huang, D. D. Yuan, H. Z. Zhang, Y. L. Cao, G. R. Li, H. X. Yang and X. P. Gao, *RSC Adv*., **2013**, 3, 12593.
30. S.-Y. Chung, J. T. Bloking and Y.-M. Chiang, *Nature Mater*., **2002**, 1, 123.
31. J. Qu, L. Shi, C. He, G. Gao, B. Li, Q. Zhou, H. Hu, G. Shao, X. Wang and J. Qiu, *Carbon*, **2014**, 66, 485.
32. V. Aravindan, M. V. Reddy, S. Madhavi, S. G. Mhaisalkar, G. V. Subba Rao, and B.V.R. Chowdari, *J. Power Sources*, **2011**, 196, 8850.
33. B. Senthilkumar, K. Vijaya Sankar, R. Kalai Selvan, D. Meyrick and M. Minakshi, *RSC Adv*, **2013**, 3, 352.
34. D. Ghosh, S. Giri, Md. Moniruzzaman, T. Basu, M. Mandal and C. K. Das, *Dalton Trans.*, **2014**, 43, 11067.
35. A. Langrock, Y. Xu, Y. Liu, S. Ehrman, A. Manivannan and C. Wang, *J. Power Sources*, **2013**, 223, 62.
36. M. Minakshi, S. Duraisamy, P. Tirupathi Rao, S. Kandhasamy and N. Munichandraiah, *Int. J. Electrochemical Sci*., **2014**, 9, 5974.
37. K. Bhattacharya and P. Deb, *Dalton Trans.*, **2015**, 44, 9221.
38. J. Huang, B. G. Sumpter and V. Meunier, *Angew. Chem. Int. Ed*., **2008**, 47, 520.
39. J.W. Lee, M. S. Park, B. Anass. J. H. Park, M. S. Palika and S. G. Doo, *Electrochim. Acta*, **2010**, 55, 4162.
40. K. Sathiyaraj, G. Babu, D. Bhuvaneswari and N. Kalaiselvi, *Ionics*, **2011**, 17, 49.
41. Handbook of X-ray Photoelectron Spectroscopy, Physical Electronics Division, Perkin Elmer Corporation, USA (1992).
42. Y. Xia, M. Wei and Y. Lu, *Synth. Met*., **2009**, 159, 372.
43. S. Lim and J. Cho, J. *Electrochem. Commun*., **2008**, 10, 1478.

Dalton Transactions Accepted Manuscript

44. G. G. Amatucci, F. Badway, A. Du Pasquier and T. Zheng, *J. Electrochem. Soc*., **2001**, 148, A930.
45. B. E. Conway, *J. Electrochem. Soc*., **1991**, 138, 539.
46. M. Minakshi, S. Baskar, M. Ionescu (Unpublished report).
47. M. Q. Wu, G. A. Snook, G. Z. Chen and D. J. Fray, *Electrochem. Commun*., **2004**, 6, 499.
48. Q. Liang, L. Ye, Z.-H. Huang, Q. Xu, Y. Bai, F. Kang and Q.-H. Yang, *Nanoscale* **2014**, 6, 13831.
49. X. Fan, C. Yu, Z. Ling, J. Yang and J. Qiu, *ACS Appl. Mater and Interfaces*, **2013**, 5, 2104.
50. J. Yin, L. Qi and H. Wang, *ACS Appl. Mater and Interfaces*, **2012**, 4, 2762.
51. S.-M. Oh, S. –T. Myung, J. Hassoun, B. Scrosati and Y.-K. Sun, *Electrochem. Commun*., **2012**, 22, 149.
52. Y.-K. Sun, S.-T. Myung, M.-H. Kim, J. Prakash and K. Amine, *J. Am. Chem. Soc*., **2005**, 127, 13411.
53. H. Kim, G. Yoon, I. Park, K.-Y. Park, B. Lee, J. Kim, Y.-U. Park, S.-K. Jung, H.-D. Lim, D. Ahn, S. Lee, and K. Kang, *Energy Environ. Sci.* **2015**, DOI: 10.1039/C5EE01876E.
54. T. Cottineau, M. Toupin, T. Delahaye, T. Brousse and D. Belanger, *Appl. Phys. A*, **2006**, 82, 599.
55. P. L. Taberna, P. Simon and J. F. Fauvarque, *J. Electrochem. Soc.*, **2003**, 150, A292.
56. B. G. Choi, J. Hong, W.H. Hong, P. T. Hammond, H. S. Park, *ACS Nano*, **2011**, 5, 7205.
57. M. W. Wu, D. D. Zhao, S. J. Bao and H. L. Li, *J. Solid State Electrochem*. **2007**, 11, 1101.
58. M. Ghaemi, F. Ataherian, A. Zolfaghari and S. M. Jafari, *Electrochim. Acta*, **2008**, 53, 4607.
59. R. Ding, L. Qi and M. Jia, *Electrochim. Acta,* **2013**, 107, 494.
60. M. D. Stoller, S. J. Park, Y. W. Zhu, J. H. An and R. S. Ruoff, *Nano Lett*., **2008**, 8, 3498.

Dalton Transactions Accepted Manuscript

Table 1 The crystal structural parameters of *m*-$NaFePO_4$ calculated by using different values of U parameters and compared with those obtained from experimental values.

Cell parameter	U=0 eV (GGA)	U=3.71 eV ref [24]	U=5.3 eV	Experimental values from ref [24]
a	5.024	5.038	5.047	5.0434
b	6.847	6.845	6.846	6.8679
c	8.977	9.013	9.021	8.9773
E_g	0	2.99	3.84	-
Volume/cell	308.802	310.832	311.704	310.951

Table 2 Average TM-TM distances of *m*-$NaMn_{1/3}Co_{1/3}Ni_{1/3}PO_4$ in Angstrom.

	Mn-Mn	Co-Co	Ni-Ni	TM-TM_avg
C1	3.376	3.384	3.377	3.379
C2	3.383	3.383	3.384	3.383
C3	5.965	5.864	5.846	5.891

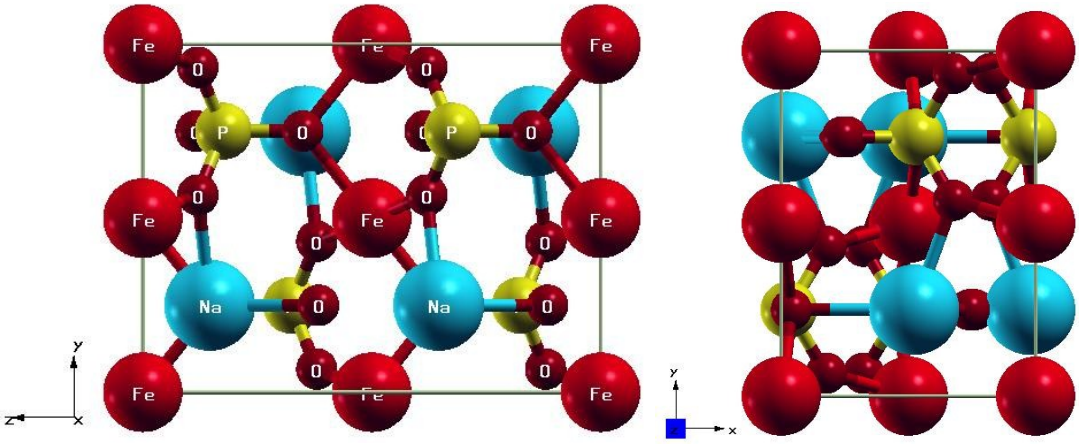

Figure 1 Illustration of *m*-$NaFePO_4$ (maricite) structure in Side and Bird's Eye view perspective respectively. Atomic species are labeled corresponding to ball colors as displayed. Na, Fe, P and O spheres are represented with spheres of decreasing size.

Dalton Transactions Accepted Manuscript

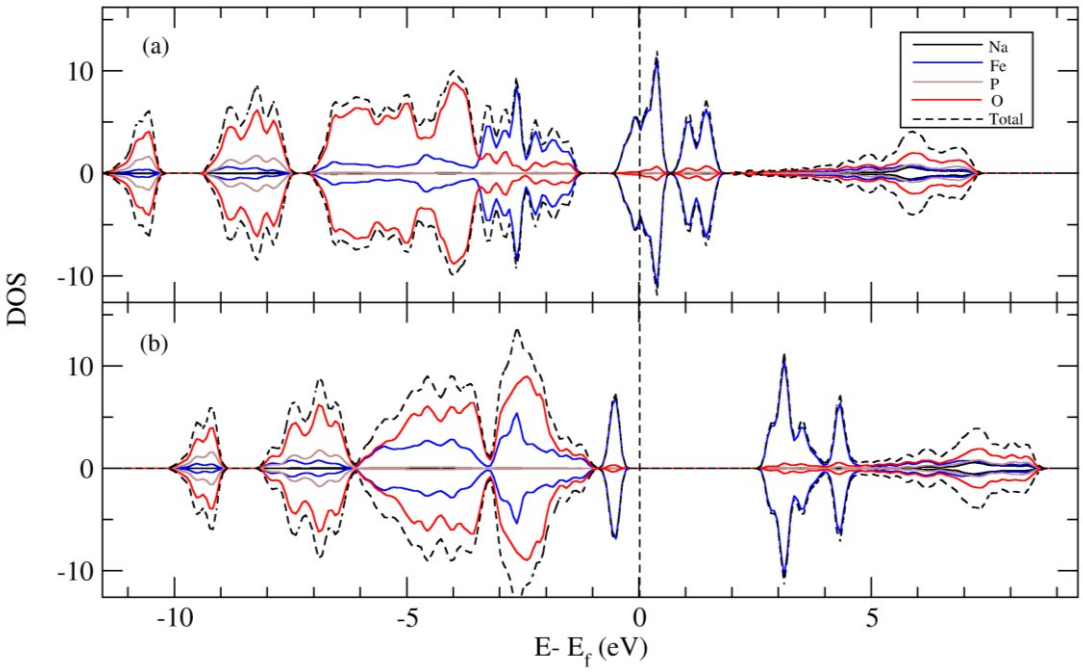

Figure 2 The density of states of *m*-$NaFePO_4$ using (a) PBE type GGA (U_{Fe} = 0 eV) and (b) PBE type GGA+U calculations (U_{Fe}= 3.71 eV). The Fermi level has been set at 0 eV.

Dalton Transactions Accepted Manuscript

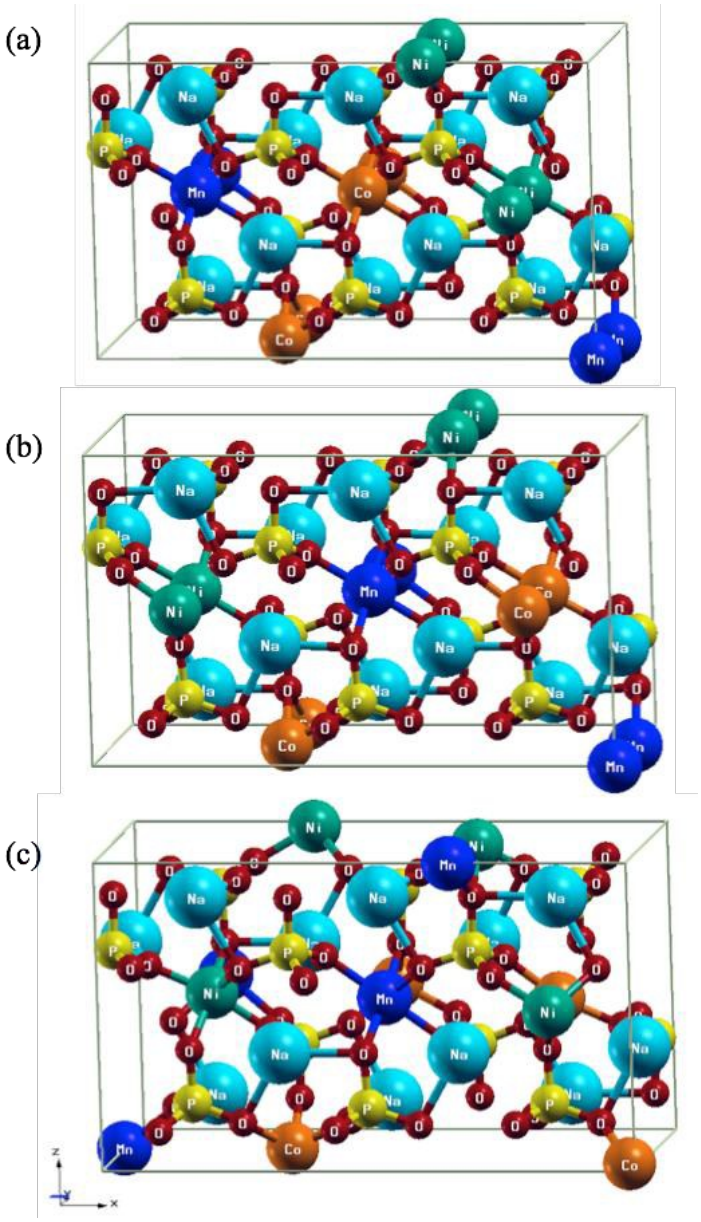

Figure 3 The optimized iso-structures of mixed maricite, *m*-$NaMn_{1/3}Co_{1/3}Ni_{1/3}PO_4$ obtained from three different configurations, namely (a) C1 (b) C2 and (c) C3 that we simulated in this work by considering the difference in TM-TM distances.

Dalton Transactions Accepted Manuscript

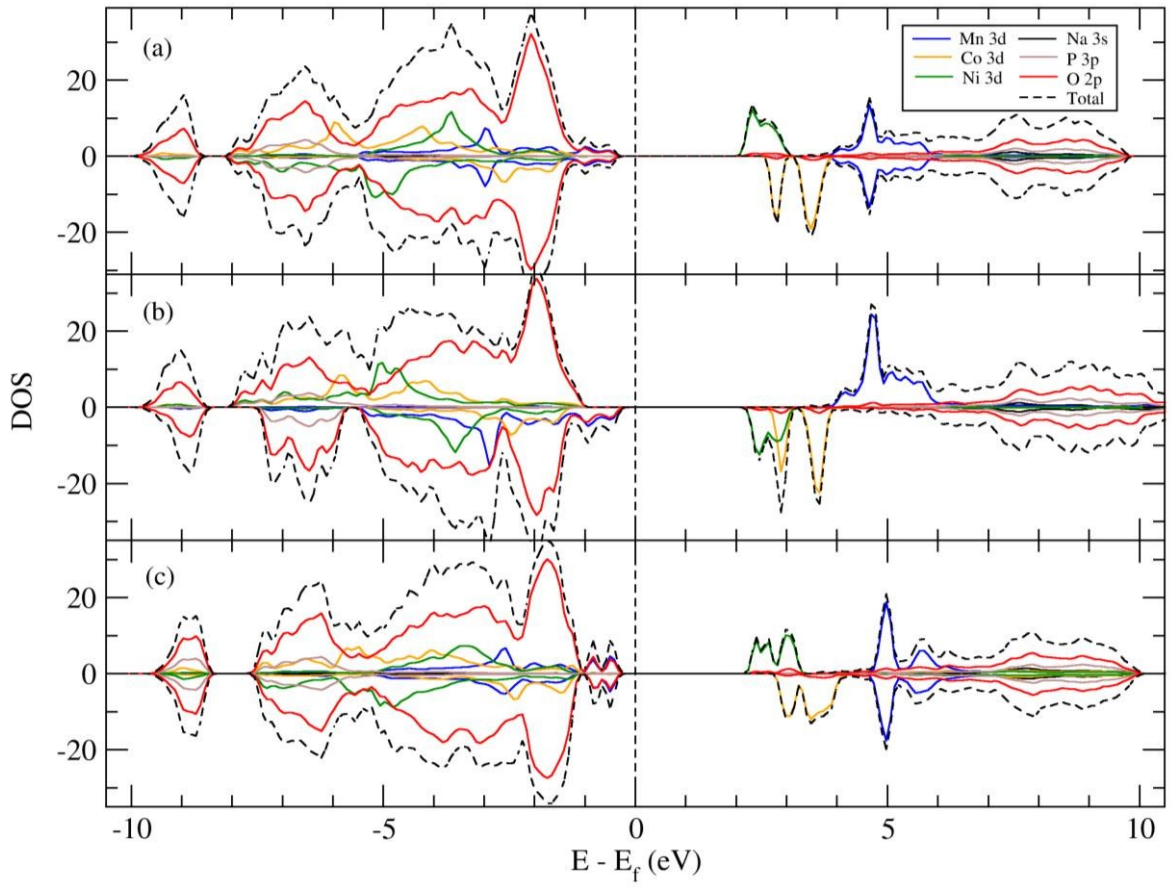

Figure 4 The total DOS (dash line) and orbital-decomposed DOS for each element (solid line) of (a) C1, (b) C2, and (c) C3 configuration of *m*-$NaMn_{1/3}Co_{1/3}Ni_{1/3}PO_4$ obtained from GGA+U calculations.

Dalton Transactions Accepted Manuscript

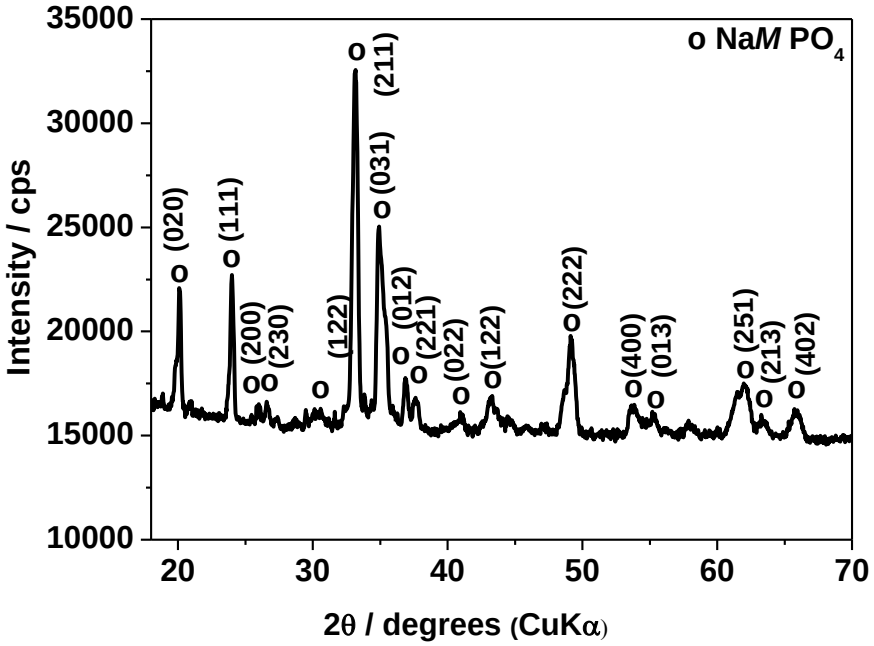

Figure 5 X-ray diffraction (XRD) patterns of as-synthesized maricite $NaMn_{1/3}Co_{1/3}Ni_{1/3}PO_4$ powder with hkl indexes of major reflection peaks marked with reference to the available database; Na*M*PO_4 (*M* = Fe).

Dalton Transactions Accepted Manuscript

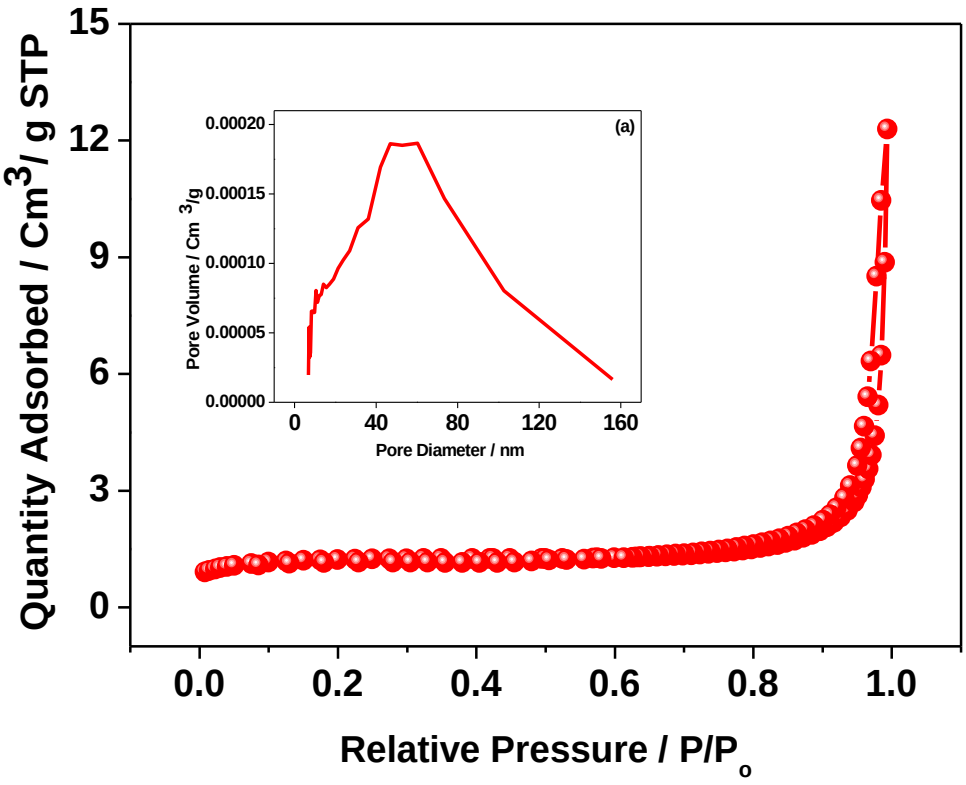

Figure 6 Nitrogen adsorption-desorption isotherms of as-synthesized *m*-$NaMn_{1/3}Co_{1/3}Ni_{1/3}PO_4$ powder. Pore size distributions of these composites are shown in the inset.

Dalton Transactions Accepted Manuscript

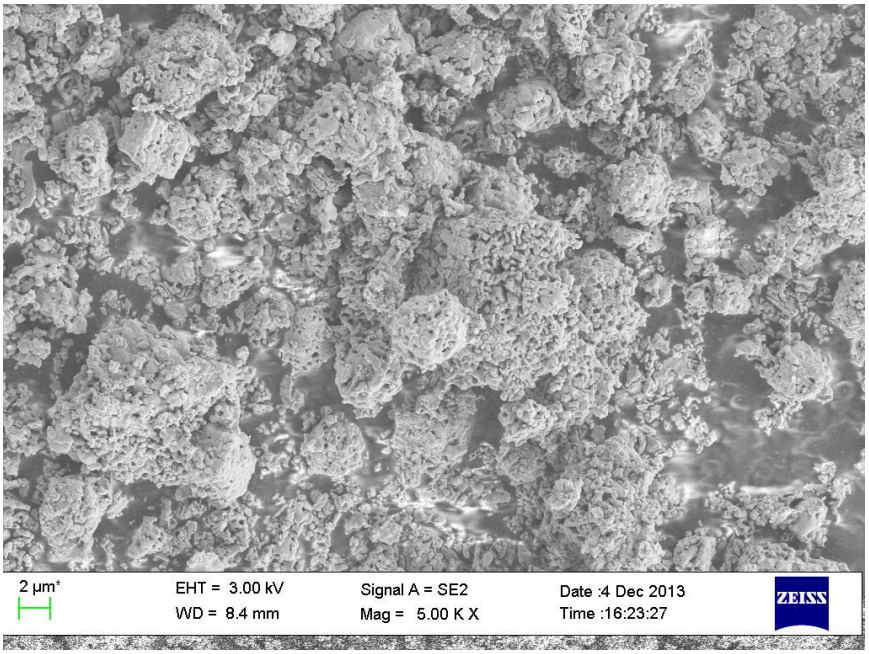

(a)

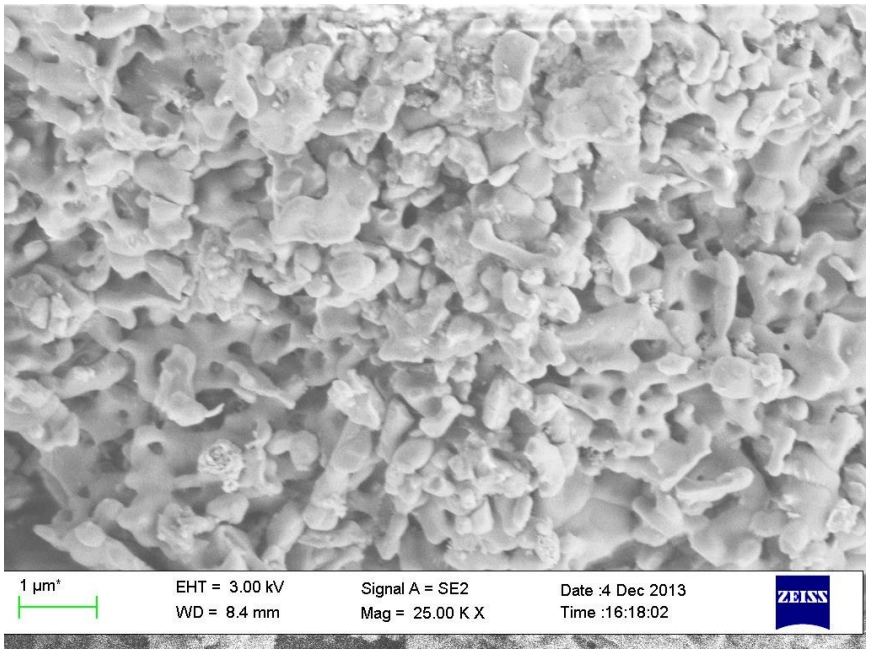

(b)

Figure 7 Scanning electron micrographs (SEM) of as-synthesized *m*-$NaMn_{1/3}Co_{1/3}Ni_{1/3}PO_4$ powder samples with different magnifications.

Dalton Transactions Accepted Manuscript

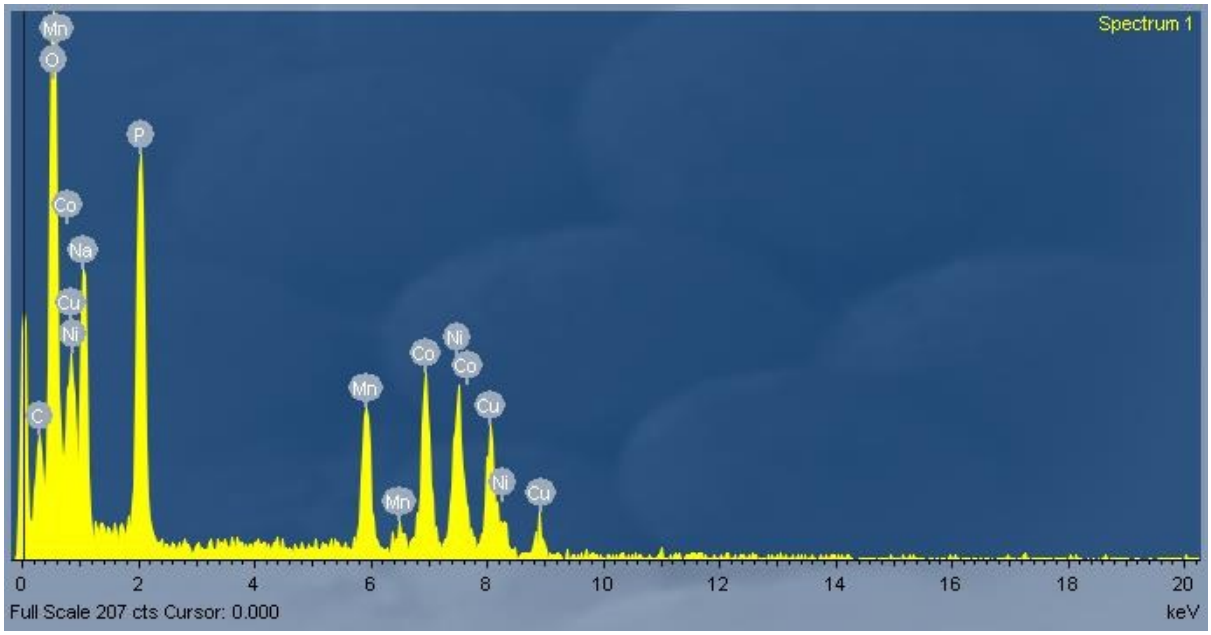

Figure 8 Energy Dispersive X-ray Spectroscopy (EDS) analsysis of as-synthesized *m*-$NaMn_{1/3}Co_{1/3}Ni_{1/3}PO_4$.

Dalton Transactions Accepted Manuscript

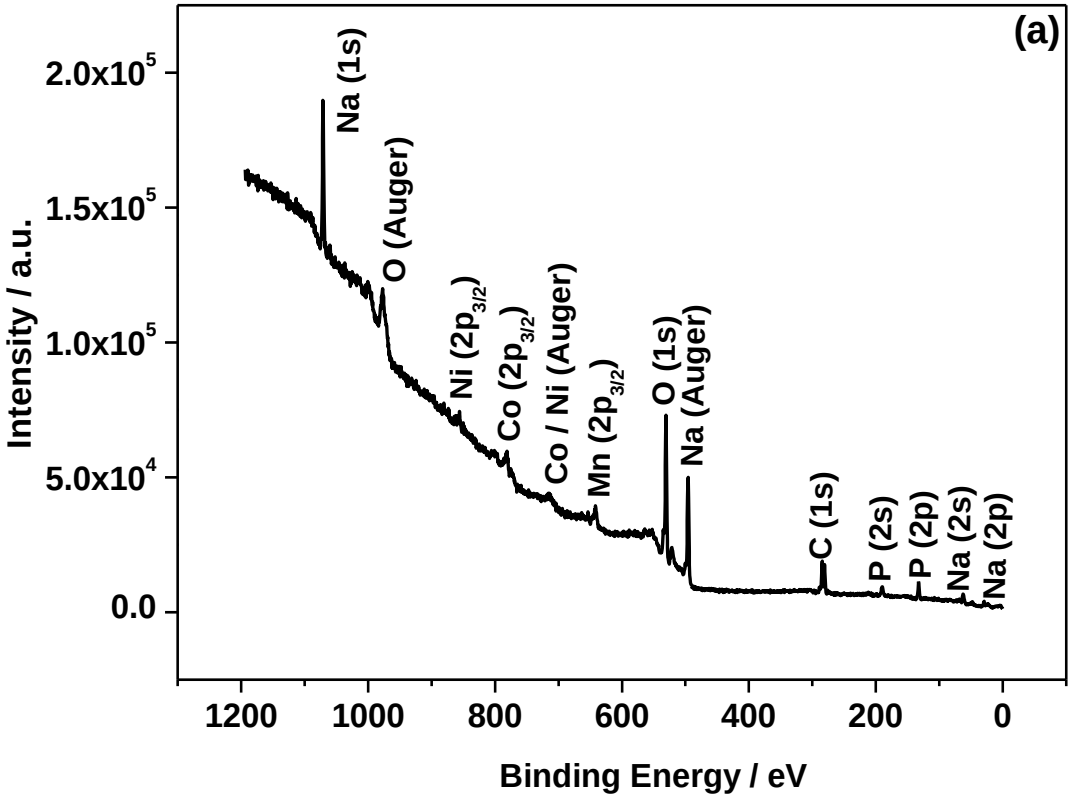

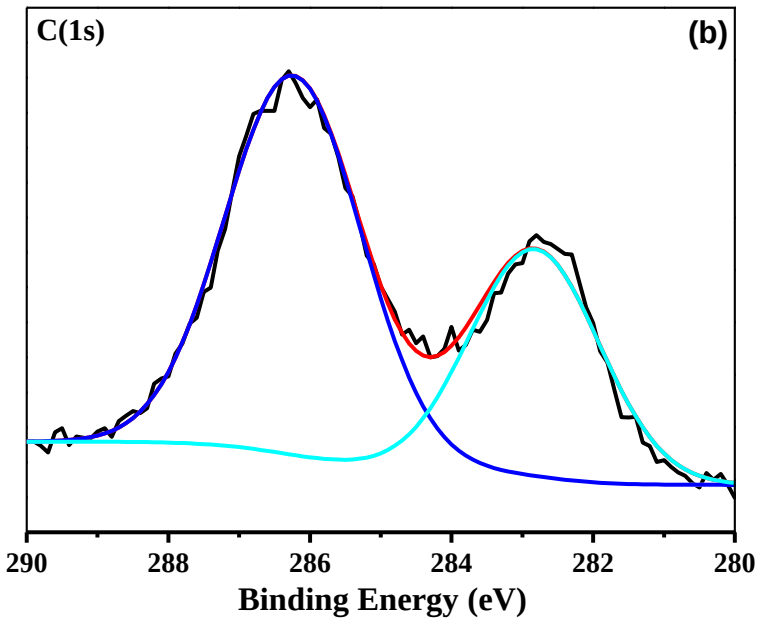

Figure 9 XPS profiles showing (a) wide scan and (b) narrow scan (C1s core level) of as-synthesized *m*-$NaMn_{1/3}Co_{1/3}Ni_{1/3}PO_4$ powder samples.

Dalton Transactions Accepted Manuscript

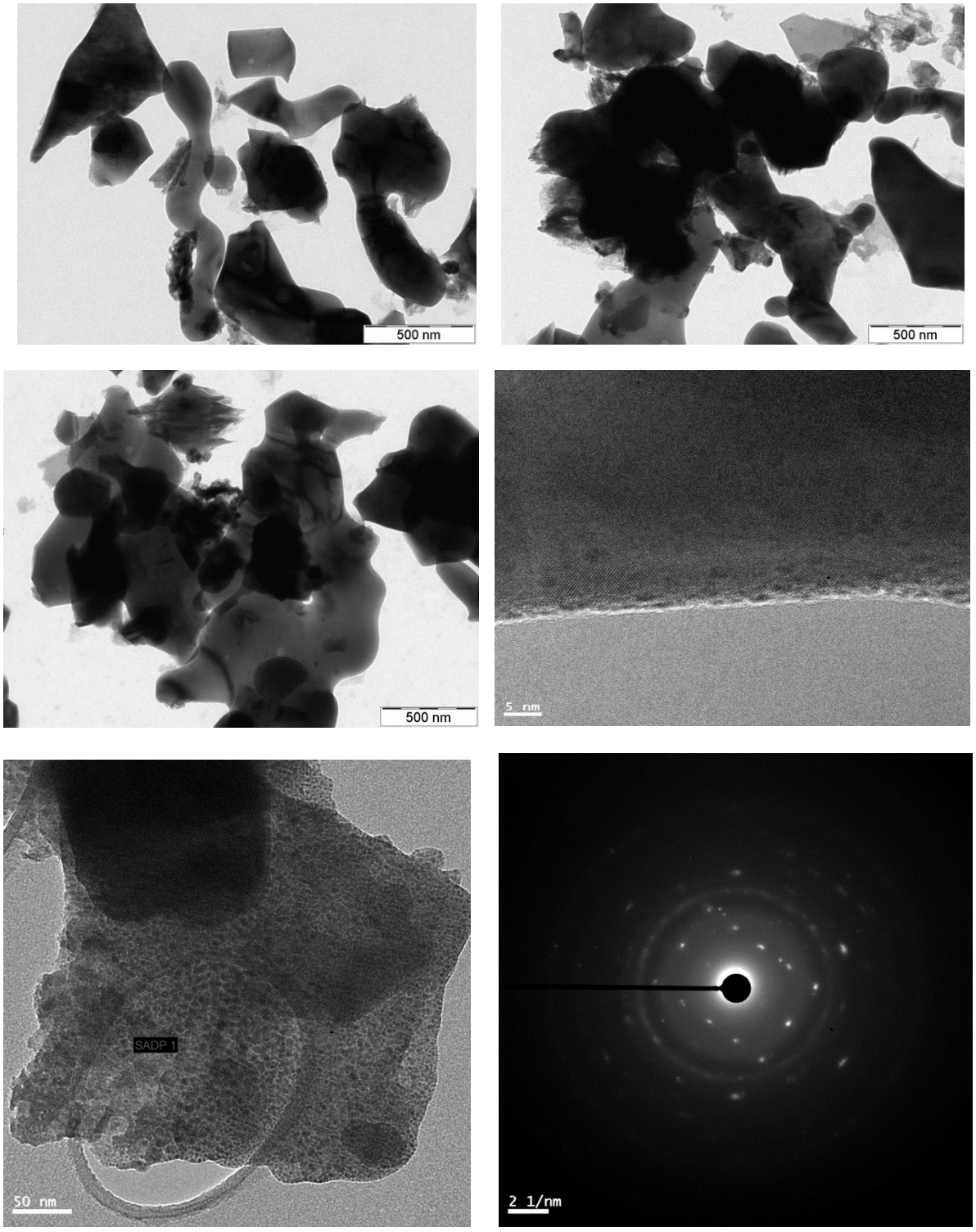

Figure 10 Transmission electron microscope (TEM) images of as-synthesized *m*-$NaMn_{1/3}Co_{1/3}Ni_{1/3}PO_4$ powder samples under different magnifications. The high-resolution TEM (HRTEM) image shows lattice fringes indicating a crystalline in nature. The bottom image (on left) at a different location representing carbon particles on the surface evidenced by selected area diffraction pattern (on right) indicating series of rings and bright spots.

Dalton Transactions Accepted Manuscript

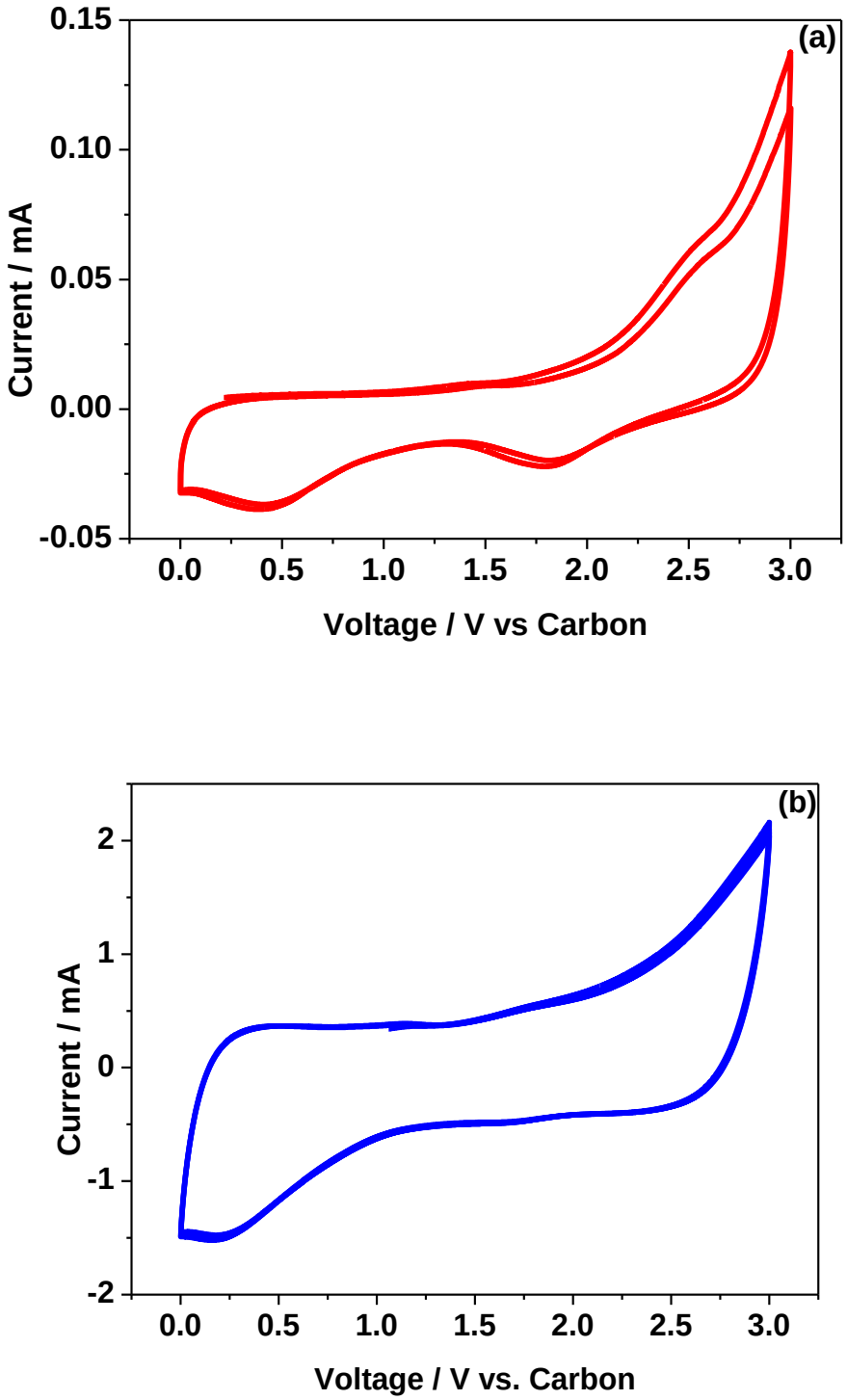

Figure 11 Cyclic Voltammogram (CV) of as-synthesized olivine *m*-$NaMn_{1/3}Co_{1/3}Ni_{1/3}PO_4$ electrode versus commercial carbon in 1M $NaPF_6$ dissolved in ethylene carbonate, diethyl carbonate and dimethyl carbonate (2:1:2 v/v) non-aqueous electrolyte at a scan rate of (a) 1 , and (b) 100 mV/s. Y-axes in the figures are different.

Dalton Transactions Accepted Manuscript

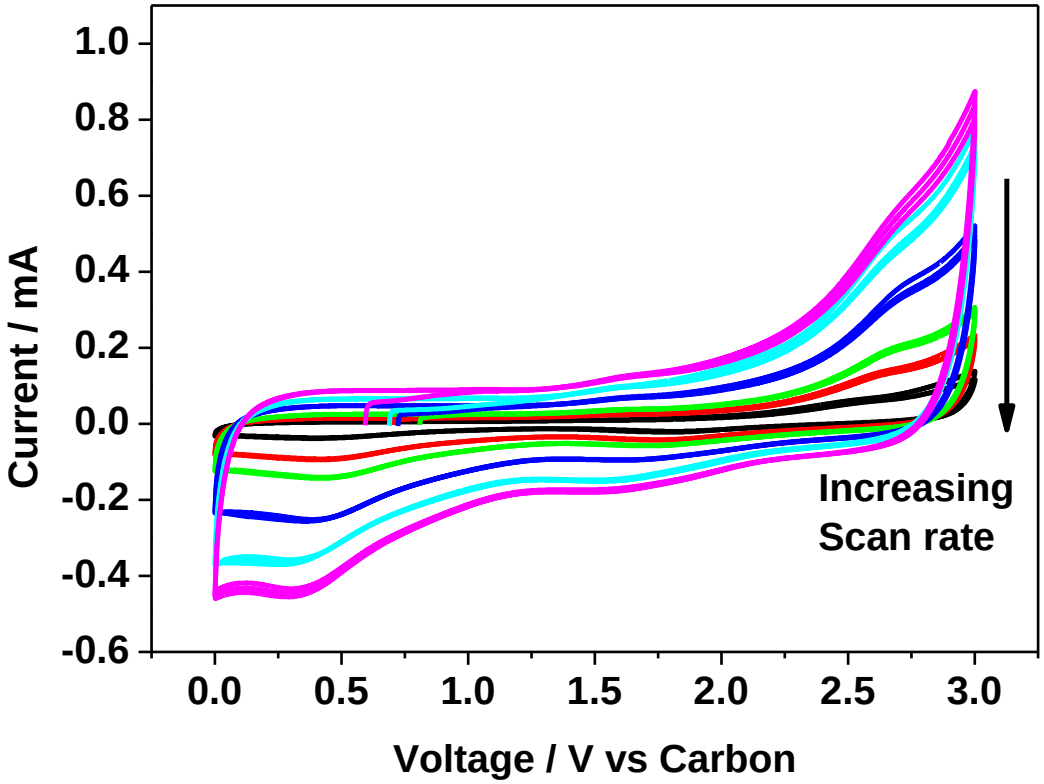

Figure 12 The rate capability behaviour of as-synthesized *m*-$NaMn_{1/3}Co_{1/3}Ni_{1/3}PO_4$ electrode versus Commercial Carbon (two electrode configuration) in 1M $LiPF_6$ dissolved in ethylene carbonate, diethyl carbonate and dimethyl carbonate (2:1:2 v/v) non-aqueous electrolyte at different sweep rates (1, 2, 5, 10, 20, 50 and 100 mV/s) from top to bottom in the curve.

Dalton Transactions Accepted Manuscript

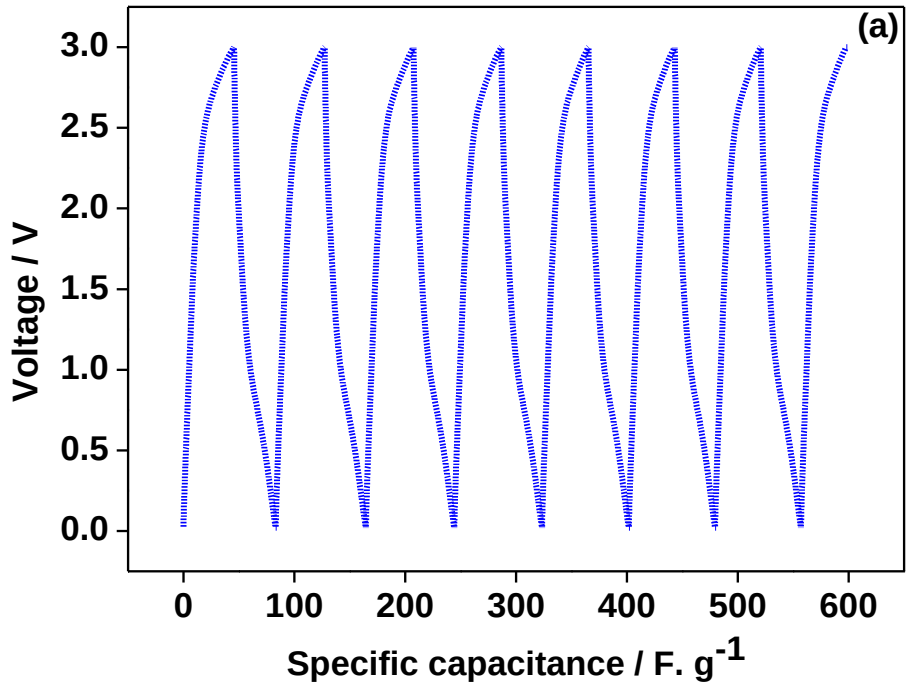

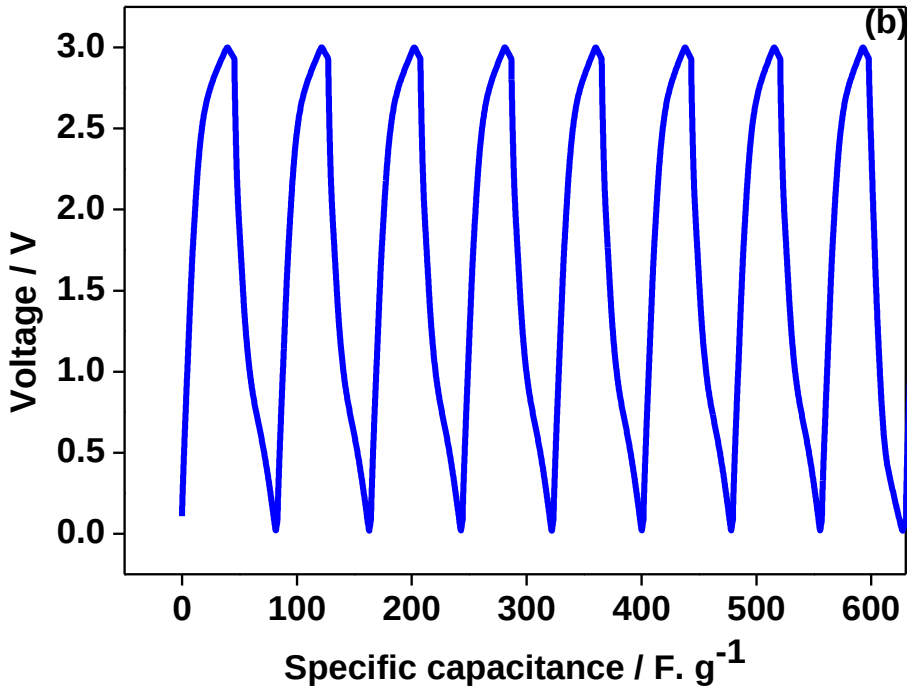

Dalton Transactions Accepted Manuscript

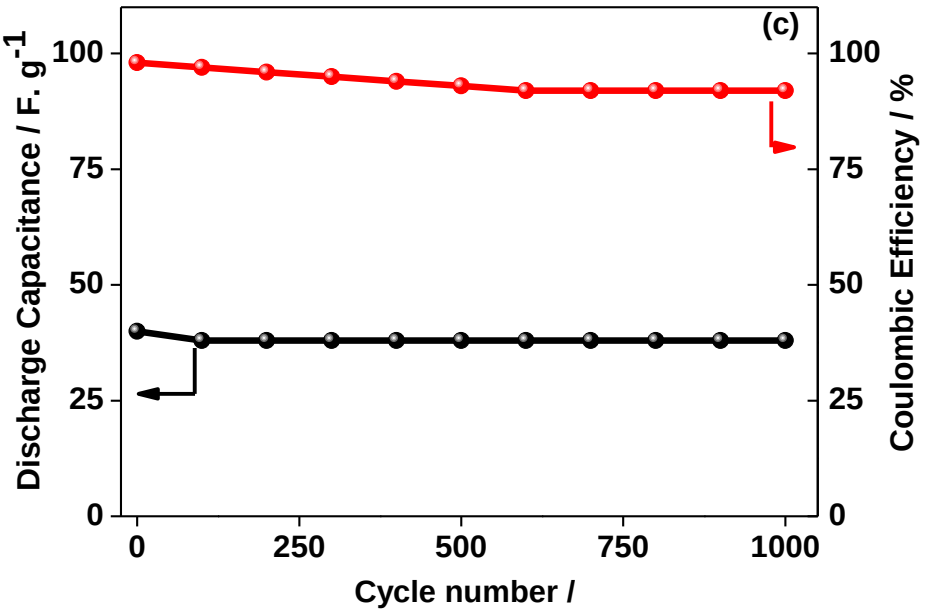

Figure 13 Voltage vs. time of as-synthesized *m*-$NaMn_{1/3}Co_{1/3}Ni_{1/3}PO_4$ electrode versus Carbon in 1M $NaPF_6$ dissolved in ethylene carbonate, diethyl carbonate and dimethyl carbonate (2:1:2 v/v) non-aqueous electrolyte at a constant current of 0.12 A/g. 16 (a-b) shows a voltage profile with consistent capacitance values for first 100 and last 100 cycles (before 1000 cycles) respectively, (c) shows the cell performance during multiple cycling.

Dalton Transactions Accepted Manuscript

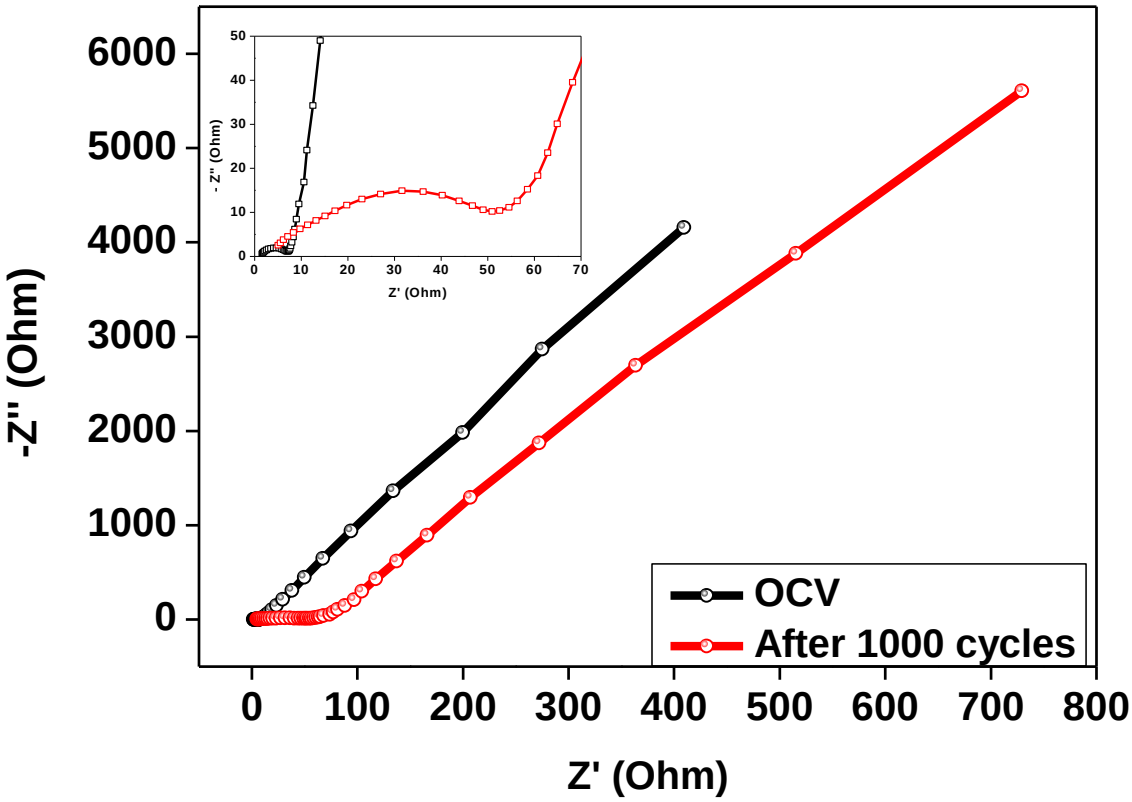

Figure 14 Nyquist plots as-synthesized *m*-$NaMn_{1/3}Co_{1/3}Ni_{1/3}PO_4$ electrode versus Carbon (a) during open circuit voltage and (b) after 1000 cycles.

Dalton Transactions Accepted Manuscript

ToC

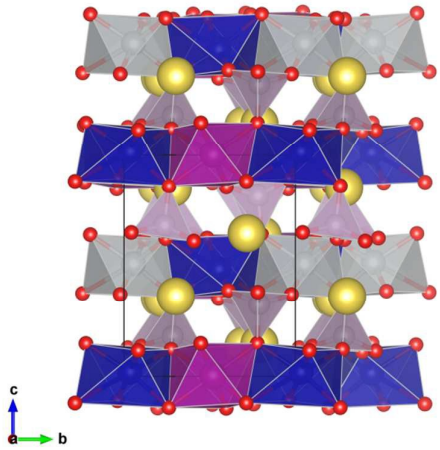

Most stable configuration of *m*-$NaMn_{1/3}Co_{1/3}Ni_{1/3}PO_4$ as an electrode for hybrid capacitor. The distorted octahedra of Ni-O, Co-O, Mn-O and P-O tetrahedron are represented in grey, blue, purple and magenta respectively. O and Na are in red and yellow colours, respectively.

Dalton Transactions Accepted Manuscript